



Experimental characterization of hydrogen adsorption sites for H/W(111) using low energy ion scattering

Chun-Shang Wong ^{1,*} Josh A. Whaley,¹ Z. J. Bergstrom ² Brian D. Wirth,^{2,3} and Robert D. Kolasinski^{1,†}

¹Sandia National Laboratories, Livermore, California 94551, USA

²University of Tennessee, Knoxville, Tennessee 37996, USA

³Oak Ridge National Laboratory, Oak Ridge, Tennessee 37830, USA



(Received 30 September 2019; revised manuscript received 18 November 2019; published 5 December 2019)

Low energy ion scattering (LEIS) and direct recoil spectroscopy (DRS) are among the few experimental techniques that allow for the direct detection of hydrogen on a surface. The interpretation of LEIS and DRS measurements, however, is often made difficult by complexities that can arise from complicated scattering processes. Previously, these complexities were successfully navigated to identify the exact binding configurations of hydrogen on a few surfaces using a simple channeling model for the projectile ion along the surface. For the W(111) surface structure, this simple channeling model breaks down due to the large lateral atomic spacing on the surface and small interlayer spacing. Instead, our observed hydrogen recoil signal can only be explained by considering not just channeling along the surface but also scattering from subsurface atoms. Using this more complete model, together with molecular dynamics (MD) simulations, we determine that hydrogen adsorbs to the bond-centered site for the W(111)+H(ads) system. Additional MD simulations were performed to further constrain the adsorption site to a height $h = 1.0 \pm 0.1 \text{ \AA}$ and a position $d_{BC} = 1.6 \pm 0.1 \text{ \AA}$ along the bond between neighbors in first and second layers. Our determination of the hydrogen adsorption site is consistent with density functional theory simulation results in the literature.

DOI: [10.1103/PhysRevB.100.245405](https://doi.org/10.1103/PhysRevB.100.245405)

I. INTRODUCTION

Hydrogen-metal interactions are important for many energy applications, such as hydrogen storage [1] and infrastructure [2], as well as plasma-facing components in fusion reactors [3]. For fusion, tungsten is one of the leading plasma-facing material candidates. Key issues for hydrogen-tungsten interactions include hydrogen blistering [4,5], hydrogen embrittlement [6,7], and tritium retention and inventory [3,8–10]. To convincingly address these matters requires a fundamental understanding of how hydrogen initially adsorbs onto the tungsten surfaces before ultimately diffusing into the bulk. Hydrogen adsorption on low-index tungsten surfaces has been modeled using density functional theory (DFT) simulations [11,12]. However, there is a lack of experiments to validate DFT predictions for the most complex of the low-index tungsten surfaces, W(111).

Detection of hydrogen is a daunting challenge for most conventional surface analysis techniques. Auger [13,14] and x-ray photoelectron [15] spectroscopies (XPS) do not provide direct sensitivity to chemisorbed hydrogen (although in specialized cases, XPS can detect slight peak shifts that arise from H bonding). As for the main structural techniques of surface science, scanning tunneling microscopy [16] (STM), and low energy electron diffraction [17] (LEED), the signal from the hydrogen itself is often overwhelmed by the substrate. This

is particularly true in cases where the surface reconstructs. With these techniques, definitive detection of hydrogen has been achieved under limited circumstances. Temperature programmed desorption (TPD) is a precise means to detect total hydrogen coverage [18], but information about binding sites and energies is often ambiguous. Vibrational spectroscopies, such as electron energy loss spectroscopy [19] (EELS) and Fourier transform infrared (FTIR) spectroscopy [20], can provide insight into the hydrogen bonding configuration, though interpreting the vibrational spectra from these techniques is often challenging. Helium atom scattering [21,22] (HAS) is sensitive to changes in surface corrugation induced by adsorbed hydrogen, as demonstrated by the successful determination of the hydrogen adsorption sites for several crystalline surfaces [23–26]. In addition to identifying hydrogen superstructures on surfaces, HAS is also completely nondestructive, is applicable to metals and insulators alike, and is sensitive to extremely dilute adsorbates. However, modeling the surface corrugation changes to determine precise hydrogen adsorbate locations and the corresponding bond lengths is challenging, especially when the surface undergoes reconstruction [24]. Furthermore, certain hydrogen adsorption geometries can be particularly difficult to characterize, such as when adsorbed hydrogen atoms are located close to one another [23] or are located near the surface [27].

While there is no single solution to the difficulties mentioned above, low energy ion beam techniques offer several strengths for detecting chemisorbed hydrogen. Low energy ion scattering (LEIS) and direct recoil spectroscopy (DRS) rely on low energy ion beams to probe the composition and

*chuwong@sandia.gov

†rkolasi@sandia.gov

structure of surfaces. Early works [28,29] illustrated the use of surface channeling to identify hydrogen binding positions. Bastasz *et al.* [28] used an approach in which He^+ was scattered from chemisorbed D in the far-forward direction at small scattering angles. Since then, advances in measurement and analysis techniques have allowed for hydrogen adsorption sites to be identified for W(100) [30], W(110) [11,31], and Be(0001) [32], using a model based on the surface channeling of projectile ions. Surface channeling occurs due to the extreme glancing angle of projectile ions relative to the surface, which allows projectile ions to be guided by surface atoms along prominent azimuthal channels. If hydrogen adsorption sites are located within such a channel, the hydrogen recoil signal at that azimuthal angle would be expected to be large. This surface-channeling model was used to interpret multi-angle hydrogen recoil maps to determine whether hydrogen adsorption sites were located within each azimuthal channel. Despite this progress, the main disadvantage of the low energy ion beam techniques is the complexity of the scattering processes, which can make the analysis of the measurements difficult.

In this work, we extend the use of multiangle scattering and recoil maps to characterize the W(111)+H(ads) system. The W(111) surface structure was captured with LEIS, while the hydrogen adsorption site was identified with DRS. The scattering and recoil measurements were modeled by and agreed well with molecular dynamics (MD) simulations. Additional MD simulations were performed to constrain the hydrogen adsorbate positions and heights. Our determination of the H adsorption site and its location are in good agreement with DFT predictions in the literature [12], providing strong experimental validation.

The bare W(111) surface structure has some distinctive features as compared to the surfaces previously studied with LEIS and DRS, as it features large lateral distances between surface atoms, with small interlayer spacing. For example, as compared to W(100), nearest neighbors in the surface monolayer of W(111) are about 40% further apart, and the interplanar distance between monolayers for a bulk-terminated W(111) surface is also about 40% shorter. The short interplanar distance is further exacerbated by relaxation of the bare W(111) surface. According to DFT simulations [12,33,34], the interplanar distance between the first and second layers, as well as for the second and third layers, are reduced by a further 20%, a rather sizable amount.

The distinctive features of the W(111) surface structure lead to multiangle scattering and recoil maps for the W(111)+H(ads) system that require more complex interpretations than previously studied surfaces [11,30,35,36]. These previous works yielded multiangle maps whose features could be well explained by scattering processes with the top monolayer of the substrate and any adsorbed hydrogen. However, the open and shallow surface structure of W(111) allows W atoms in deeper layers to play a major role in scattering processes so that their contributions to scattering and recoil signals can no longer be ignored. This complication can be addressed in a straightforward manner for the forward-scattering maps; however, this complication is more challenging to address for the hydrogen recoil map, as the simple surface-channeling model cannot adequately describe the recoil

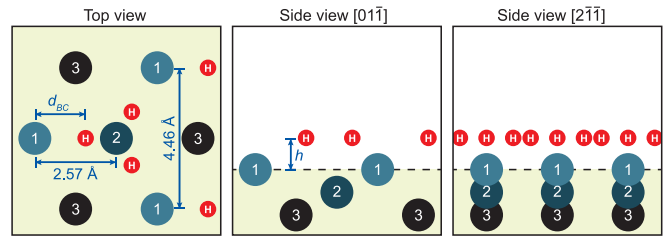


FIG. 1. Illustration of the bond-centered (BC) hydrogen adsorption site predicted by the DFT simulations of Bergstrom *et al.* [12]. The large circles indicate positions of W atoms (the numerals specify the layer), while the smaller red circles denoted “H” indicate the positions of the BC adsorption site. The adsorption location of the hydrogen is defined by the height h and lateral position d_{BC} along the bond between nearest neighbors in the first and second layers.

signal. We find that for W(111), the channeling model needs to include not just channeling *along* the surface (which increases the H recoil signal), but also channeling *into* the surface (which decreases the H recoil signal). Both competing effects play roles in determining the structure of the multiangle recoil maps.

Another complication is that the configuration of surface atoms on W(111) also allows for a high level of H coverage with a complex binding geometry. Experimental flash desorption measurements by Tamm *et al.* [37] indicated that a coverage of at least $\Theta = 4$ was possible at sufficiently low temperatures (<78 K), where Θ is the number of adsorbed H per W atom in the surface monolayer. This observation has been supported by recent DFT results of Bergstrom *et al.* [12]. The DFT simulations [12] also predict that the most energetically favorable adsorption site is the bond-centered (BC) site, located above the bond between the first- and second-layer W atoms. An illustration to depict the BC site is presented in Fig. 1. At low coverage ($\Theta = 0.25$), the BC site is predicted to be at a height $h = 0.96$ Å above the surface, with a lateral position $d_{BC} = 1.69$ Å. The predicted lateral position is closer to the second layer W atom than the first layer W atom, so that the adsorption site is nearly equidistant to both W atoms when height is taken into account. At full coverage of the BC site ($\Theta = 3$), both the height and lateral positions are expected to shift slightly to $h = 1.12$ Å and $d_{BC} = 1.49$ Å, respectively. The second and third most energetically favorable adsorption sites are predicted to be the BC2 site (along bonds between second- and third-layer W atoms) and the top site (T). Adsorption to the BC2 site is only expected after the BC site is largely filled, while adsorption to the T site is not expected.

II. EXPERIMENTAL METHODS

Experimental measurements were performed with an angle-resolved ion energy spectrometer (ARIES). A mass-separated beam was produced using a Colutron ion source. The source ionized the source gas (typically He or Ne) by electron bombardment. The beam was initially focused using an Einzel lens, passed through a Wein filter for velocity selection, and then sent through a series of apertures. The ions were

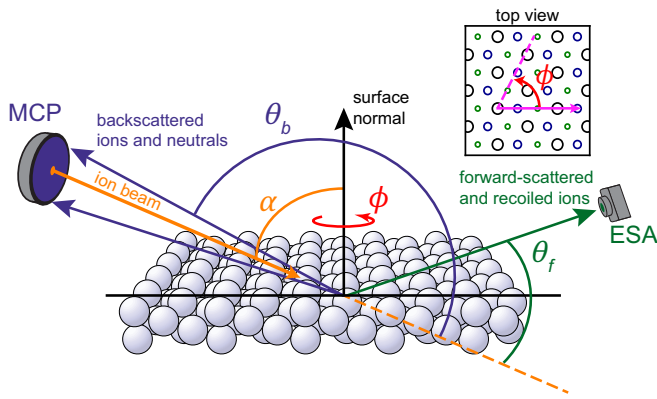


FIG. 2. Coordinate system and illustration of the experiment. The ion beam was at an angle of incidence α relative to the surface normal. The W(111) crystal could be rotated azimuthally in ϕ relative to the ion beam. The crystallographic orientation is depicted in the inset: first-layer W atoms are drawn as the large black circles, second-layer W atoms as the smaller blue circles, and third-layer W atoms as the smallest green circles. For our coordinate system, $\phi = 0$ corresponds to the $[2\bar{1}\bar{1}]$ direction. In the forward-scattering direction, an electrostatic analyzer (ESA) detected scattered and recoiled ions for a chosen forward-scattering angle θ_f . In the backscattering direction, a multichannel plate was used to perform impact-collision ion scattering spectroscopy (ICISS) measurements.

then deflected through a mechanical bend to remove neutral particles. A final Einzel lens enabled focusing of the beam to a 0.5 mm spot at the sample surface. A set of deflection plates near the exit of the ion source allowed for rastering of the beam in a rectangular pattern (typically 2×2 mm), with the raster amplitude adjusted to correct for changes in incidence angle to ensure a constant exposure area. Forward-scattered and recoiled ions were detected using an electrostatic analyzer (ESA). As an alternative, ARIES could also be configured to perform backscattering measurements with a multichannel plate. Further details on the experimental apparatus can be found in Ref. [38].

The angles used to describe ion scattering and recoil in ARIES are illustrated in Fig. 2. The angle of incidence (or polar angle) α of the beam on the sample was defined from the sample's surface normal. The scattering (or recoil) angle θ was defined relative to the ion beam direction. Finally, the azimuthal angle ϕ defined the rotational orientation of the crystal with respect to the ion beam and detector.

Our W sample was a single crystal of 8 mm diameter (MaTecK) that was ground to within 0.1° of the (111) crystal plane. The sample was fastened to the manipulation stage with a tantalum wire about its perimeter to avoid undesirable ion shadowing or blocking effects. The uncertainty in alignment of the polished surface relative to the ion beam (α) was verified using a laser to be $<1^\circ$. The amount of hydrogen on the W(111) sample surface was controlled by varying the amount of hydrogen in the measurement chamber. The measurement chamber had a base pressure of 9×10^{-10} Torr, primarily due to residual H_2 . The pressure within the measurement chamber was maintained at 3×10^{-8} Torr while the Colutron ion source was active by differential pumping. The hydrogen coverage on the W(111) surface could be increased

by introducing $H_2(g)$ into the chamber through a variable leak valve, as there is no dissociation barrier for H to adsorb onto W. Saturation hydrogen coverage for room temperature was achieved with a H_2 partial pressure of 1×10^{-7} Torr.

III. ARIES MEASUREMENTS

LEIS and DRS were performed with ARIES using 1- and 3-keV Ne^+ beams with an ESA positioned in the forward-scattering direction. The ESA had an acceptance aperture with a 2-mm diameter and was positioned 18.5 mm away from the sample, corresponding to a 6° angular diameter. Ion energy spectra were obtained by sweeping the ESA detection energy from 0 to E_0 , the projectile ion energy. The ESA measures only ion energy, without taking ion mass into account, so that the spectra contained contributions from both scattered and recoiled ions.

For crystalline lattices, additional structural details can be extracted by building multiangle maps of scattering and recoil measurements [30,35,36,39]. These multiangle maps take advantage of the fact that the energy of scattered and recoiled ions depends only on θ and not ϕ or α . This allows the ϕ and α dependence of specific scattering and recoil processes to be investigated by varying ϕ and α while monitoring a specified energy E/E_0 for a chosen θ . These maps often provide more insight into how scattering processes are affected by the surface structure as compared to measurements for a fixed α or a fixed ϕ .

A. Ion energy spectra

Representative ion energy spectra for residual H and with $H_2(g)$ dosing are presented in Fig. 3 for various α . The ESA was positioned at a fixed $\theta_f = 45^\circ$, while the W(111) crystal was aligned at $\phi = 60^\circ$. Peaks in the spectra are found near the expected energies for elastic collisions [40], $E/E_0 = 0.090$, 0.353, 0.493, and 0.937 for H(R), O(QS), O(R), and W(QS), respectively. The observed peaks were typically at slightly lower energies due to inelastic effects. Here, we adopt the standard notation [41] that X(R) indicates a recoiled ion of species X, X(QS) indicates a projectile ion that has undergone quasisingle scattering off an atom of species X, and X(DS) indicates double scattering.

There are, however, some complications in the scattering and recoil peaks. For smaller α , the H(R) signal has two maxima: a larger peak at $E/E_0 = 0.061$ and a smaller peak near $E/E_0 = 0.110$. There are also additional peaks at $E/E_0 = 0.830$ and $E/E_0 = 0.950$. These complications in peak structure have been identified and explained for other W surfaces by Bastasz *et al.* [42] and Kolasinski *et al.* [30,31]. The dual H(R) peaks arise from a multicollision recoil process where either the incident Ne^+ undergoes a collision with a W atom before recoiling the H or the incident Ne^+ recoils the H into a W atom. Similarly, the enhanced tail near $E/E_0 = 0.950$ is due to double scattering of Ne^+ off W, W(DS). For both cases, at more glancing α , the binary collision approximation breaks down so the corresponding peaks become less distinct. On the other hand, the peak near $E/E_0 = 0.830$ arises from Ne^+ scattered off W with energy losses from collisions with H. This is evident as the peak becomes much larger and elongated for conditions where collisions with H are more significant

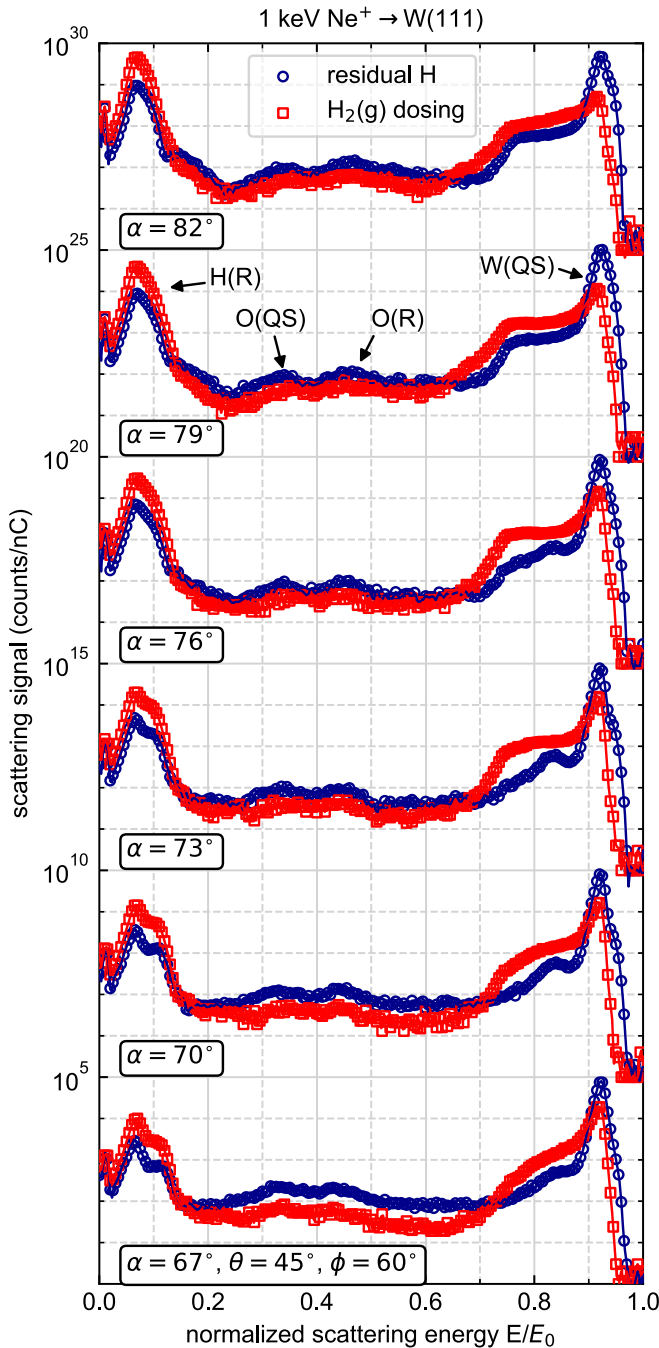


FIG. 3. Ion energy spectra at various α for residual H (blue circles) and $\text{H}_2(\text{g})$ dosing (red squares) at a partial pressure of 2×10^{-7} Torr. The ion energy on the horizontal axis has been normalized by the projectile ion energy of 1 keV. For clarity, spectra are offset vertically.

[larger α and $\text{H}_2(\text{g})$ dosing]. This Ne^+ energy-loss mechanism has been confirmed [31] with binary collision approximation simulations using MARLOWE [43].

B. Multiangle LEIS maps

Multiangle scattering maps of the W(QS) signal were constructed for 3- and 1-keV Ne^+ beams. The ESA was

positioned at $\theta_f = 45^\circ$ for both maps, and it monitored the observed W(QS) peaks at $E/E_0 = 0.928$ for the 3-keV Ne^+ map and $E/E_0 = 0.920$ for the 1-keV Ne^+ map. Polar and azimuthal angles were varied in the ranges $50.0^\circ \leq \alpha \leq 80.5^\circ$ and $0^\circ \leq \phi \leq 360^\circ$ to construct a 21×181 grid. As done by Agostino *et al.* [35], each value of α was converted to the physical distance at which the shadow cone intercepts the surface. This conversion allows the multiangle maps to be rendered in real space, so that the scattering intensity pattern can be compared to the position and shadow lines of surface layer W atoms. The positions and shadow lines of subsurface W atoms can also be compared in a similar manner, as explained in the Supplemental Material [44], which also includes further discussions on shadow cones and shadow lines.

The multiangle W(QS) scattering map for 3-keV $\text{Ne}^+ \rightarrow \text{W}(111)$ is presented in Fig. 4(a). The defining features of this map are the six regions with large scattering signals that appear in approximately 60° intervals. At first, the scattering intensity pattern appears to arise from the sixfold symmetric nature of the first-layer W atoms. However, a closer inspection at larger α (larger d) reveals that the scattering map is actually threefold symmetric, with an additional reflectional symmetry about the center of each 120° segment. This scattering intensity pattern suggests that second- and third-layer W atoms are participating in the scattering process.

The multilayer scattering can be identified by overlaying the positions of the salient W atoms from the first three layers and their shadow lines on the scattering maps, as shown in Fig. 4(a). The shadow lines [35,36,44], which delineate the regions where Ne^+ is expected to be scattered, align extremely well with regions of high scattering signal. The regions with the largest scattering intensity correspond to angles at which there are ion focusing contributions from two second-layer W atoms and a third-layer W atom. Furthermore, as expected, at the smallest distances (closest to normal incidence), the scattering intensity is dominated by contributions from W atoms in deeper layers. Conversely, at the largest distances (at more glancing angles), the W atoms nearer to the surface begin to play a larger role. These observations reveal that the six regions with large amounts of scattering arise not from the six nearest neighbors within the top monolayer but rather from the first three neighbors in each of the second and third layers. As such, the map is not sixfold symmetric like the top monolayer. Instead, the map has the same symmetry as the first three layers of the W(111), a threefold rotational symmetry with a reflectional symmetry about each 120° section. Molecular dynamics simulations performed with Kalypso [45] confirmed that the W(QS) signal arises primarily due to scattering off the first three W layers. These simulation results are provided in the Supplemental Material [44].

The scattering intensity map for the 1-keV Ne^+ beam, Fig. 4(b), yields similar conclusions. The map for the 1-keV Ne^+ beam exhibits the same symmetries as before, and scattering by subsurface atoms needs to be considered to fully describe the scattering intensity pattern. There are, however, two notable differences that arise from the lower projectile ion energy. First, the scattering intensity profile can be well described by the shadow lines for just the first two layers

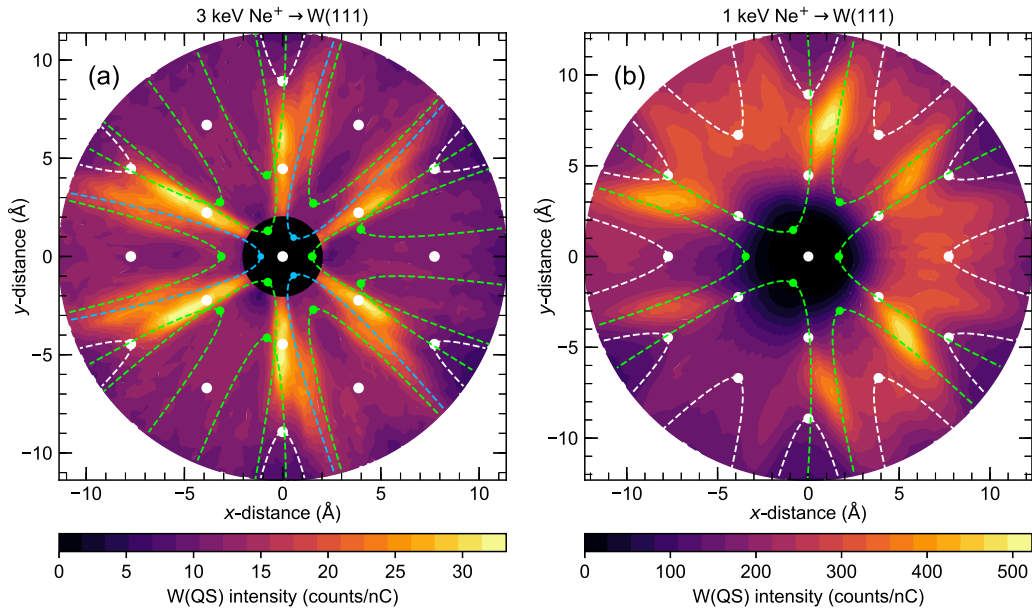


FIG. 4. Scattering intensity maps of the W(QS) peak using (a) 3-keV Ne^+ and (b) 1-keV Ne^+ beams, where lighter colors indicate regions with greater relative scattering intensity. These maps were obtained by varying the azimuthal angle ϕ and angle of incidence α . These angles, α and ϕ , have been converted to physical distances along the surface plane [35], so that the positions of W atoms can be indicated by circles overlaid on the scattering maps. The positions of surface layer W atoms are given by the largest circles (white), while second- and third-layer W atoms are represented by the smaller green and blue circles, respectively. Smaller circle size indicates increasing depth. Shadow lines [44] drawn from W atom positions delineate regions where enhanced ion scattering is expected. These regions correspond well with the obtained scattering intensity patterns.

of W atoms, because the lower energy Ne^+ do not penetrate as deeply into the substrate. Second, the scattering intensity features are less sharply defined, a result of the larger shadow cone radius for 1-keV $\text{Ne}^+ \rightarrow \text{W}$.

C. Multiangle DRS maps

Experimental DRS measurements taken with ARIES were used to construct multiangle H(R) maps. Maps for the W(111) sample exposed to only residual H, as well as with $\text{H}_2(\text{g})$ dosing at a partial pressure of 2×10^{-7} Torr, are presented in Fig. 5. For both maps, the ESA was positioned at $\theta_f = 45^\circ$ and monitored the H(R) peak at $E/E_0 = 0.088$. DRS measurements were taken at 181 values of ϕ in the range $0^\circ \leq \phi \leq 360^\circ$ for each of 20 values of α in the range $72^\circ \leq \alpha \leq 84^\circ$.

The maps for residual H and dosed $\text{H}_2(\text{g})$ are very similar. Like the W(QS) maps, both contain a threefold rotational symmetry with a reflectional symmetry for each 120° section. The H(R) signal generally increases with α , with minima at $\phi = 0^\circ, 120^\circ$, and 240° . Between each of these primary minima, there are a set of three peaks. The central peak, located at $\phi = 60^\circ, 180^\circ$, and 300° , remains at the same azimuthal position as α changes. On the other hand, the other two peaks shift azimuthally toward the central peak as α increases.

Besides absolute magnitudes, the primary difference between the residual H and dosed $\text{H}_2(\text{g})$ maps are the relative intensities of the peaks and minima. To highlight these differences, we compare the ϕ variation in the H(R) signal between the residual H and dosed $\text{H}_2(\text{g})$ measurements for $\alpha = 76^\circ$ in

Fig. 6. Most notably, the H(R) signal for $\text{H}_2(\text{g})$ dosing has a larger relative signal along the $\langle 2\bar{1}\bar{1} \rangle$ directions ($\phi = 0^\circ, 60^\circ, 120^\circ, 180^\circ, 240^\circ$, and 300°).

The H(R) signal for the W(111)+H(ads) system cannot be fully explained by the simple surface-channeling model that was successfully applied to W(100) [30], W(110) [11,31], and Be(0001) [32]. There are two unique features of the H(R) maps for the W(111)+H(ads) system not seen for these simpler surfaces. First, the H(R) signal does not have a 180° reflectional symmetry in ϕ . This lack of symmetry indicates that the scattering and recoil processes were not equivalent along each direction of a single azimuthal channel. Second, the H(R) peaks near the $\langle 10\bar{1} \rangle$ directions are not symmetric about the azimuthal channels, and the peaks are not necessarily centered on the channeling direction.

The reflectional asymmetry in the H(R) signal along the $\langle 2\bar{1}\bar{1} \rangle$ directions can be explained by taking into account not just channeling *along* the surface but also channeling *into* the surface. An indication of the likelihood for Ne^+ to be channeled into the W(111) surface as opposed to along the surface can be estimated using impact-collision ion scattering spectroscopy (ICISS) backscattering measurements [46]. Minima in the backscattered ICISS signal correspond to high likelihoods of channeling into the surface. Using the setup and methodology described in Ref. [39], we performed an ICISS backscattering measurement for 3-keV $\text{Ne}^+ \rightarrow \text{W}(111)$ at $\alpha = 76^\circ$. The ϕ variation in the measured signal, which is presented in Fig. 7, revealed backscattering minima at $\phi = 0^\circ, 120^\circ$, and 240° , with larger backscattering signals for the antiparallel directions of $\phi = 180^\circ, 300^\circ$, and 60° . This correlates well with the H(R) signal, suggesting that the H(R)

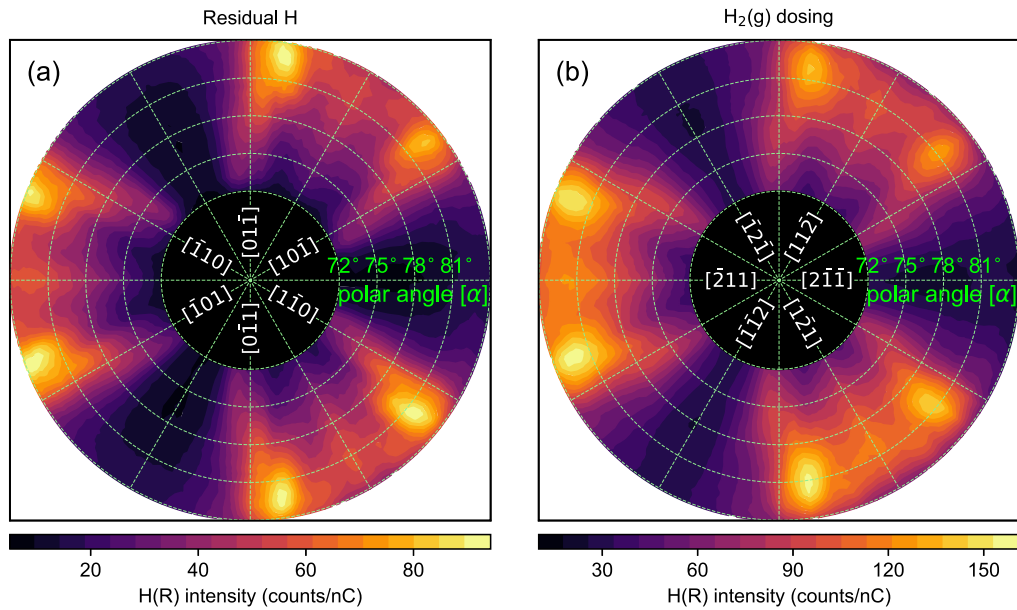


FIG. 5. Hydrogen recoil intensity maps for $E/E_0 = 0.088$ obtained with ARIES for (a) residual H and (b) a partial pressure of H_2 of 2×10^{-7} Torr. These data were acquired by varying the azimuthal angle ϕ and angle of incidence α , which correspond to polar angles and radial distances in the maps, respectively. The maps reveal similar features; both have a threefold symmetric recoil signal that increases with the angle of incidence α . The $\langle 10\bar{1} \rangle$ and $\langle 2\bar{1}\bar{1} \rangle$ directions are indicated in panels (a) and (b), respectively.

signal at $\phi = 0^\circ, 120^\circ$, and 240° is diminished in comparison to the H(R) signal at $\phi = 180^\circ, 300^\circ$, and 60° because a much larger fraction of the Ne^+ is channeled into, rather than along, the surface at those angles. Deeper within the surface, the Ne^+ are unable to recoil the adsorbed H above the surface. The lack of symmetry in the H(R) signal about the $\langle 10\bar{1} \rangle$ directions likely also arises due to multilayer scattering processes.

Despite not being able to fully describe the H(R) maps, the simple surface-channeling model can still be used to eliminate unlikely H-adsorption sites. The channeling of projectile ions

into the surface can be accounted for by noting that the presence of adsorbed H within a prominent azimuthal channel is a necessary but no longer sufficient condition for an azimuthal H(R) peak. The H(R) maps in Fig. 5 have peaks along both the $\langle 2\bar{1}\bar{1} \rangle$ and $\langle 10\bar{1} \rangle$ directions, indicating that H adsorption sites should be located within both prominent azimuthal channels. In Fig. 8, we provide top-view illustrations of high-symmetry and DFT predicted adsorption sites. The top (T) and threefold (TF) sites are unlikely adsorption sites based on the surface-channeling model, as neither contains H adsorption sites in both prominent azimuthal channels.

On the other hand, the bridge (B) and bond-centered (BC) sites appear to be very similar. Both have H adsorption sites within both prominent azimuthal channels and have a maximal coverage of $\Theta = 3$. However, there is a key difference:

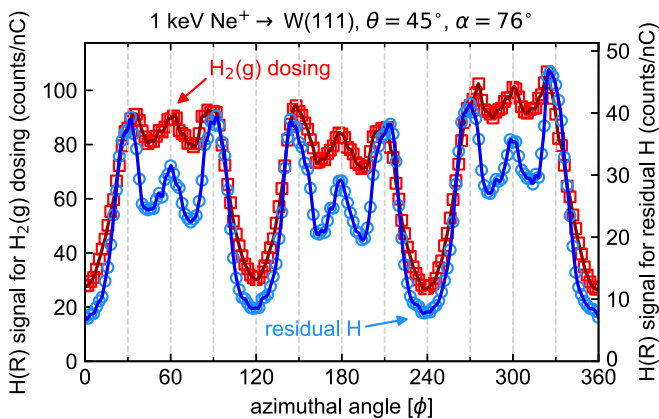


FIG. 6. Comparison of ARIES H(R) measurements at $E/E_0 = 0.088$ for residual H (blue circles) and with $\text{H}_2(\text{g})$ dosing (red squares). Aside from a larger overall signal for the dosed case (note the y-axis scales), the primary difference is that the dosed case also has larger relative peaks along the $\langle 2\bar{1}\bar{1} \rangle$ directions ($\phi = 0^\circ, 60^\circ, 120^\circ, 180^\circ, 240^\circ$, and 300°). Spline fits were drawn through the data points.

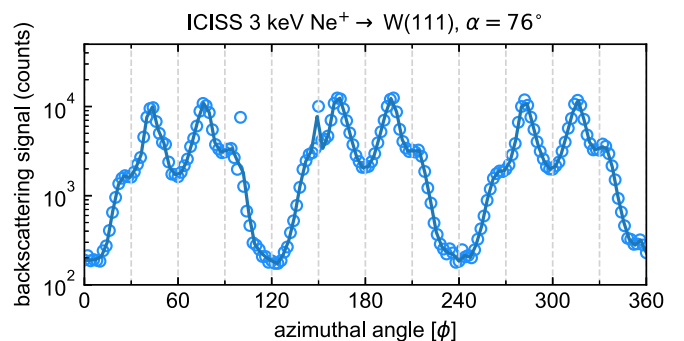


FIG. 7. ICISS backscattering measurements of W(QS) for 3-keV $\text{Ne}^+ \rightarrow \text{W}(111)$ at $\alpha = 76^\circ$. Azimuthal angles with low backscattering signals indicate a large amount of Ne^+ channeling into the surface; the angular positions of these minima ($0^\circ, 120^\circ$, and 240°) correlate well with the H(R) minima obtained from DRS.

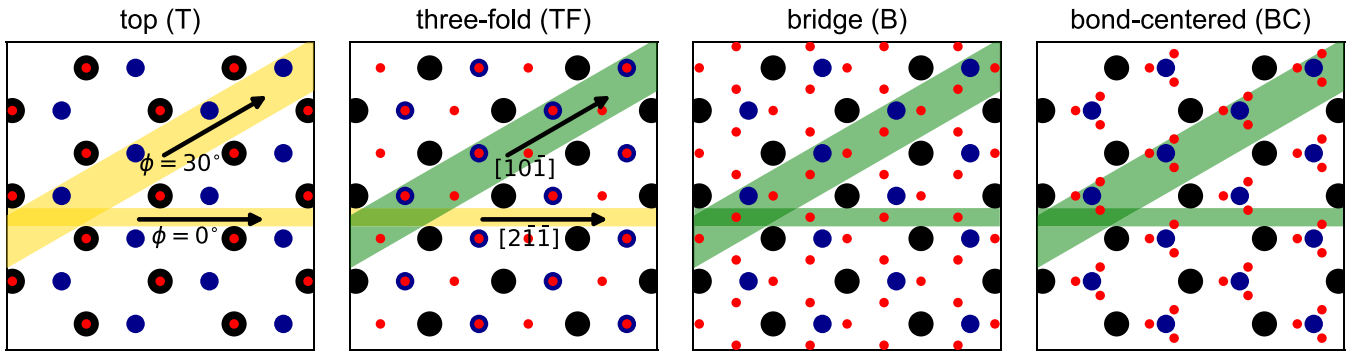


FIG. 8. Top-view illustrations of potential H adsorption sites. The large black circles represent positions of first-layer W atoms, smaller blue circles represent positions of second-layer W atoms, and the smallest red circles represent H adsorption sites. Prominent channeling azimuths are colored yellow if there are no H adsorption sites within the channel and colored green if there are H sites within the channel.

the precise H adsorption site positions within each azimuthal channel. In particular, along the $\langle 2\bar{1}\bar{1} \rangle$ azimuths, the H is adsorbed along the center of the channel for the B site, while the H are adsorbed on either side of the channel for the BC site. It was demonstrated by Kolasinski *et al.* [30] that the presence of multiple H along the exact center of an azimuthal channel leads to ion focusing effects that dechannels the projectile ion. As the H coverage increases on the surface, the dechanneling of projectile ions can cause the relative H(R) signal along the azimuthal direction to diminish. This would be the expected case for the B site. On the other hand, the BC site has triplets of H along either side of the $\langle 2\bar{1}\bar{1} \rangle$ channel, so that the opposite effect may occur. Collisions with the adsorbed H located on either side of the channel may help guide the projectile Ne^+ within the channel for a longer duration, thereby increasing the H(R) signal along that azimuthal direction.

Evidence for the enhanced channeling mechanism of the BC site can be found in the comparison of H(R) signals for residual H and $\text{H}_2(\text{g})$ dosing, shown in Fig. 6. There is a substantial increase in the relative size of the H(R) signal along the $\langle 2\bar{1}\bar{1} \rangle$ directions as the H coverage is increased, while the azimuthal positions of the peaks and minima are unchanged. The consistent positions of the peaks and minima suggest that the H(R) increase along the $\langle 2\bar{1}\bar{1} \rangle$ directions is not likely caused by surface reconstruction. Likewise, it is unlikely that the $\langle 2\bar{1}\bar{1} \rangle$ channels are being preferentially filled with adsorbed H as the coverage increases. The remaining explanation is that enhanced channeling is occurring due to adsorbed H, which provides an indication that H are being adsorbed to the BC site, not the B site.

IV. MD SIMULATIONS TO MODEL DRS MEASUREMENTS

To verify our interpretations of the experimental DRS measurements, we performed MD simulations with Kalypso [45]. First, simulations were performed to compare H(R) signals for different potential H adsorption sites (T, TF, B, and BC). After the BC site was determined to provide the best agreement with the experiment, H adsorption heights and positions were further constrained with two additional sets of simulations. All simulations were for a fixed $\alpha = 76^\circ$ and $\theta_f = 45^\circ$, while ϕ was varied in 2° increments as in the experiment. Symmetries in the substrate and adsorption sites meant that just a 60° range

in ϕ needed to be simulated; these data could be reflected and then translated to provide a full 360° description of the ϕ variation in the recoil signal. Full angular maps, with variation in α , were not simulated with Kalypso due to the required computational time.

All simulations were performed with identical W(111) substrates, while the H adsorption sites were varied. A full H layer was included for each of the potential H adsorption sites; this corresponded to $\Theta = 1$ for the T site and $\Theta = 3$ for the TF, B, and BC sites. The W(111) targets contained two W monolayers, since the LEIS scattering map, Fig. 4(b), indicated that 1-keV $\text{Ne}^+ \rightarrow \text{W}(111)$ scattering was dominated by the first two W layers. The dimensions of the W target surface was a $64 \times 32 \text{ \AA}$ rectangle. The longer dimension of 64 \AA was parallel to the azimuthal direction of the projectile; the shorter dimension was perpendicular. Modifications from a bulk W(111) lattice structure, based on DFT predictions [12], were included to better mimic experimental conditions. First, surface relaxation of the interplanar distance between the two layers of -21.8% was included. Second, vibrational displacements in the positions of the W and adsorbed H were included. These vibrational displacements were computed from a lattice temperature of 300 K and Debye temperatures Θ_D .

The Debye temperatures for the surface W and adsorbed H were obtained with DFT using the Vienna Ab-initio Simulation Package (VASP) [47,48]. A frequency analysis, described in the Supplemental Material [44], yielded $\Theta_D = 230 \text{ K}$ for a single W atom on a clean W(111) surface. For bulk W, we use the experimentally measured $\Theta_D = 310 \text{ K}$ from Clarke and Morales de la Garza [49]. The ratio between Θ_D for the surface and bulk W is consistent with experimental measurements for other low index W surfaces [49–51]. The Debye temperatures for H adsorbed to the BC site, $\Theta_D = 1992 \text{ K}$, and T site, $\Theta_D = 2519 \text{ K}$, were similarly calculated from DFT simulations based on their highest phonon frequency. Additional DFT simulations to obtain Θ_D for the TF and B sites were not performed; for these sites, $\Theta_D = 1992 \text{ K}$ was used. Details on the DFT simulations can be found in Ref. [12].

For each ϕ in the MD simulations, 1.5×10^6 independent runs were performed, in which a single 1-keV Ne^+ projectile was scattered off the W(111)+H(ads) target. The Ne^+

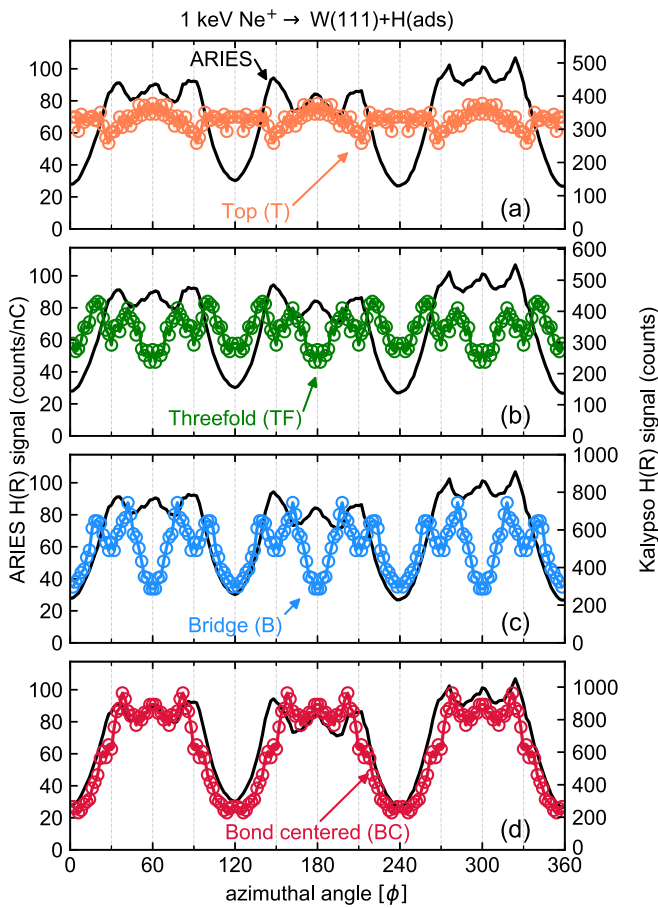


FIG. 9. Comparison of experimental DRS measurements (solid black line) to Kalypso simulations (open circles with spline fit) for different H binding sites. The DFT predicted bond-centered site agrees well with the experimental data, while other common high-symmetry sites do not. Both the experiment and simulation were for $\theta_f = 45^\circ$ and $\alpha = 76^\circ$. The adsorption heights used in these simulations were (a) 1.87 Å and [(b)–(d)] 1.0 Å.

projectile was initiated 4.6 Å above the target surface, well outside of the interaction range. Projectile-target interactions were modeled as elastic collisions using the universal potential developed by Ziegler, Biersack, and Littmark (ZBL) [52]. To keep simulation times reasonable, only projectile-target interactions were considered; target-target interactions were not included. Only H and Ne with final trajectories within a 6° angular diameter that corresponded to the angular size and position of the ESA were retained. After each simulation, the W(111)+H(ads) target was reset; damage to the target was not tracked. Further details on Kalypso and its implementation can be found in Refs. [45] and [30].

Comparisons of MD simulation results for four different H adsorption sites to experimental DRS measurements are presented in Fig. 9. Unsurprisingly, the T and TF sites show poor agreement with the DRS measurements, as their H adsorption sites do not lie in the correct azimuthal channels. The T site yielded a H(R) signal that has nearly no variation as a function of ϕ . The lack of ϕ dependence is expected as none of the T adsorption sites are located within prominent azimuthal channels, and furthermore, the DFT predicted

adsorbate height is so far above the surface (1.87 Å) that the substrate does not play a substantial role before the H is recoiled. The TF site also does not have H adsorption sites along the $\langle 2\bar{1}\bar{1} \rangle$ channels, so the TF recoil signal is also missing the experimentally observed peaks at $\phi = 60^\circ$, 180° , and 300° .

Kalypso simulations for the B site also showed poor agreement with the experimental DRS measurements, despite having H adsorption sites within the correct azimuthal channels. Unlike the experimental measurements, there are local minima along all the prominent azimuthal channeling directions (every 30°). These local minima can be attributed to the dechanneling effects that were discussed in Sec. III C. The dechanneling effect appears to be more prominent for the narrower lateral dimension of the $\langle 2\bar{1}\bar{1} \rangle$ channels, leading to a larger diminishment in the H(R) signal as compared to the $\langle 10\bar{1} \rangle$ channels.

The BC site model yielded H(R) measurements that agree well with the experiment. Just as for the experimental data, there are three primary minima in 120° intervals, starting at 0° . Each of the maxima have a series of three closely spaced peaks in roughly 25° intervals. The simulation also nearly captures the relative recoil intensities of the maxima to minima. The slight differences between the experimental and simulation results may arise from the possibility that the W(111) did not reach a $\Theta = 3$ coverage at room temperature as assumed in the simulation. Furthermore, the experimental W(111) crystal contains defects and impurities not included in the simulation model.

We next investigate the effect of adsorbate height on the H(R) signal. A series of Kalypso simulations were performed for a full H layer ($\Theta = 3$) at the BC adsorption site ($d_{BC} = 1.6$ Å) at various heights ($0.8 \text{ Å} \leq h \leq 1.4 \text{ Å}$). The spectra, presented in Fig. 10, reveal that the scattering and recoil processes are heavily dependent on the exact adsorbate height; a change in height of 0.2 Å can lead to a substantially different recoil signal. Most striking are the relative size of the signals along the $\langle 2\bar{1}\bar{1} \rangle$ channels, which increase considerably as the adsorbate height is increased. This is, again, due to the enhanced channeling of Ne^+ from the presence of H on either side of the $\langle 2\bar{1}\bar{1} \rangle$ channels. As the H adsorption height is increased, its shadowing and focusing effects on the Ne^+ projectiles are increased, leading to a more pronounced enhanced signal. This finding is consistent with previous MD modeling of the effects of H adsorbate heights on surface channeling [30]. An inspection of the plots in Fig. 10 reveal that the simulation results for an adsorbate height $h = 1.0 \pm 0.1$ Å agreed best with the experimental measurements. The uncertainty in h was determined by qualitatively comparing the simulation results to the experimental measurements.

The position of the BC adsorption site along the bond between the first- and second-layer atoms was constrained with another series of Kalypso simulations. Each simulation was performed with a full H layer ($\Theta = 3$) added at the BC adsorption site at a height $h = 1.0$ Å. The lateral position along the bond d_{BC} between the first- and second-layer W atom (as defined in Fig. 1) was varied in the range $1.3 \text{ Å} \leq d_{BC} \leq 1.9 \text{ Å}$. The results of these simulations, presented in Fig. 11, indicate that $d_{BC} = 1.6 \pm 0.1$ Å provided the best agreement with the experimental data. Just as for the obtained

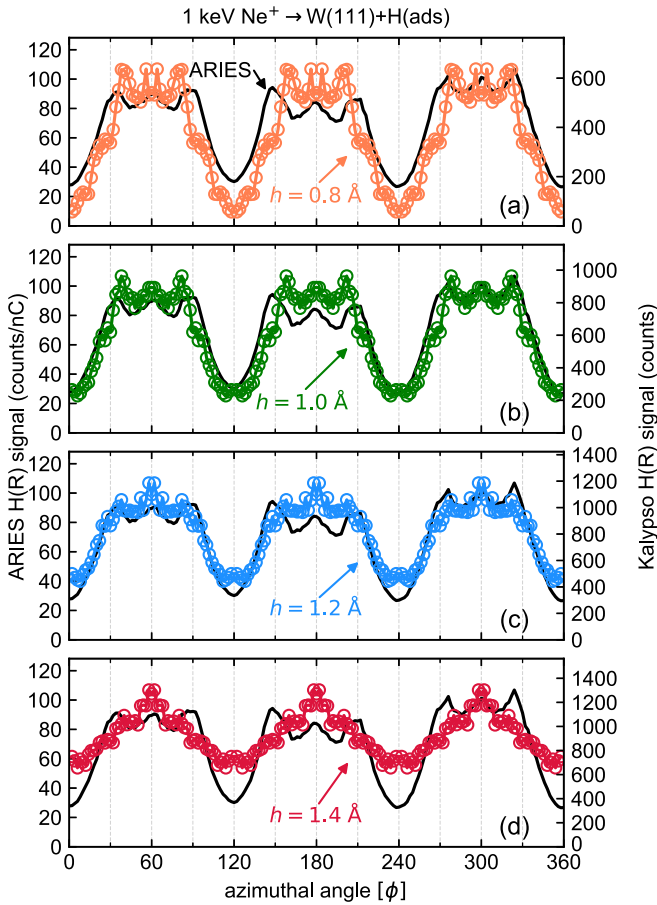


FIG. 10. Azimuthal variation of H(R) for different hydrogen adsorbate heights h obtained with MD simulations (Kalypto). Simulation data points are given as the open circles with a spline fit, whereas the experimentally measured H(R) signal is given by the black line. The adsorbate position used in these simulations was $d_{BC} = 1.6 \text{ \AA}$.

adsorbate height h , the uncertainty associated with d_{BC} is a qualitative assessment. Changes in the H(R) signal due to adsorbate position are more complicated to interpret than those due to adsorbate height, because altering the adsorbate position not only affects the channeling of the projectile Ne^+ but also whether the channeled Ne^+ can easily recoil the adsorbed H.

Reliability factors (R factors) can be used to quantify the agreement between experimental measurements and MD simulation results for different adsorbate heights and positions. We computed R factors for the MD simulation results in Figs. 10 and 11 following the procedure described in Ref. [36]. These computed R factors, which are plotted in the Supplemental Material [44], are consistent with our qualitative assessment.

Our determination of the hydrogen adsorption site location of $h = 1.0 \pm 0.1 \text{ \AA}$ and $d_{BC} = 1.6 \pm 0.1 \text{ \AA}$ is in good agreement with DFT predictions. Both of our obtained values fall between the DFT predictions for low coverage ($\Theta = 0.25$) of $h = 0.96 \text{ \AA}$ and $d_{BC} = 1.69 \text{ \AA}$ and full coverage ($\Theta = 3$) of $h = 1.12 \text{ \AA}$ and $d_{BC} = 1.49 \text{ \AA}$.

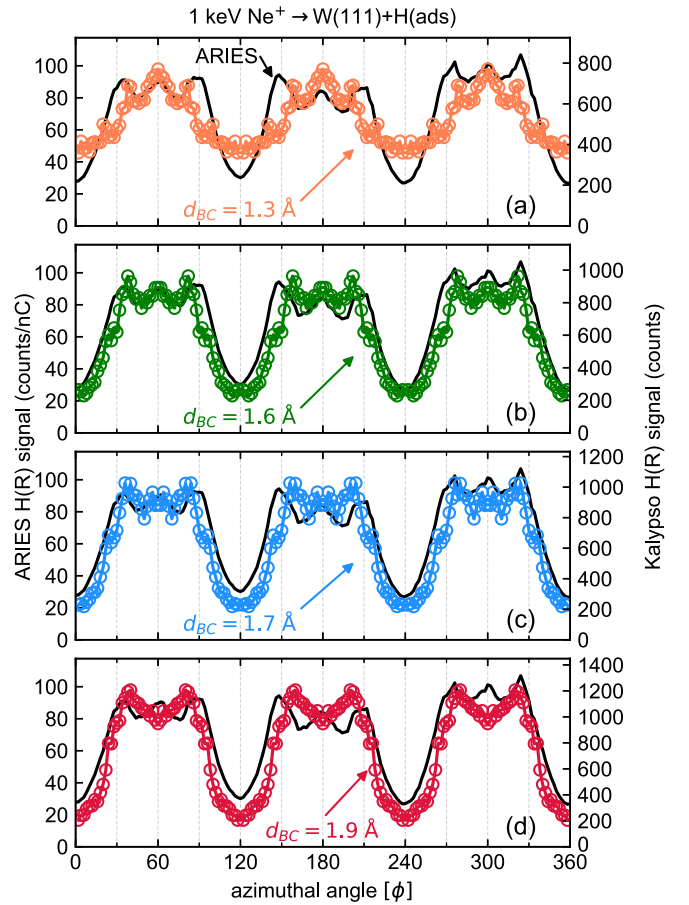


FIG. 11. H(R) obtained with MD simulations (Kalypto) for different adsorbate-positions d_{BC} . Simulation data points are the open circles with spline fits, while the experimentally measured H(R) signal is the black line. Adsorbate positions were varied in the range, $1.3 \text{ \AA} \leq d_{BC} \leq 1.9 \text{ \AA}$, while $h = 1.0 \text{ \AA}$.

V. CONCLUDING REMARKS

In this work, we demonstrated how multiangle scattering maps can be applied to complex adsorbate binding geometries with multiple substrate layers participating in the scattering process. The multilayer effects greatly complicated the multiangle scattering and recoil maps, as collisions with subsurface atoms broke otherwise expected symmetries. Shadow cone effects needed to be included for the first three substrate layers in order to characterize the scattering maps, while the simple surface-channeling model could no longer adequately describe the recoil map. Only by accounting for channeling into the surface, in addition to channeling along the surface, could the asymmetry in recoil signals along prominent azimuthal channels be explained.

A precise determination of the adsorption site locations for the complex bond-centered binding geometry required more extensive modeling with MD simulations than did previous surfaces. Unlike for high-symmetry adsorption sites, not only the adsorbate's height but also its lateral position could be varied. Our MD simulations revealed that the hydrogen recoil signal was sufficiently sensitive to variations in both the adsorbate's height and lateral position to constrain each of

their values. In particular, we discovered that the presence of hydrogen adsorbed to either side of an azimuthal channel could substantially enhance the channeling of projectile ions and, in turn, the hydrogen recoil signal along that azimuth. The extent of this enhancement was dependent on the precise location of the adsorption sites, so that the experimental and simulated hydrogen recoil signals only agreed for a small range of adsorbate heights and positions. Our constrained adsorbate height and position agree well with DFT predictions. Although our experimental results do not directly measure the H-W interaction potential, our results represent a strong validation of the DFT simulations of the H-W systems, giving confidence in DFT determinations of H-W interaction potentials.

The multiangle mapping and analysis methodology that we presented here should help extend the usefulness of LEIS and DRS to situations where multilayer scattering effects cannot be neglected. This improved methodology allows for a more complete interpretation of scattering and recoil data for ion beams with higher energies or that are incident at less glancing angles, *i.e.*, situations where incident ions penetrate more deeply into the substrate. Our work also opens the door for using LEIS and DRS to investigate a wider variety of material surfaces. First, the most direct application is for surfaces for which multilayer scattering effects are typically unavoidable, such as stepped surfaces or high-index open surfaces. Second, another application is for systems where hydrogen is thought to have subsurface adsorption sites, such as Pd(111) [53]. Hydrogen interactions with palladium are of particular interest, as the catalytic properties of palladium make it an attractive material for tritium extraction in fusion reactors [54], as well as for hydrogen storage, purification, and detection [55]. Third, these techniques may potentially be applied to investigate hydrogen adsorption on single-crystal metal alloys. Multilayer analysis of scattering maps could provide structural and compositional information of the alloy substrate, after which ion channeling studies could identify hydrogen adsorption site locations on the surface.

While our methodology was sufficient to characterize the W(111)+H(ads) system, further advancements to our modeling and experimental techniques may allow for a better characterization of a wider range of materials. To achieve determinations of the hydrogen adsorption locations with greater precision, more powerful MD simulations could be

applied to explore a more complete parameter space. With sufficient statistics, a quantitative comparison of experimental measurements to simulation results could then be made by using R factors. Further improvements to the modeling could be made by using more accurate interatomic potentials in the MD simulations than the universal ZBL potential, as corrections to the universal ZBL potential can be sizable depending on the projectile ion and target atom [56]. One potential improvement to the experimental technique could be implemented by making time-of-flight measurements in the forward-scattering direction with a multichannel plate, instead of detecting only ion energies with an electrostatic analyzer. This modification would allow for the detection of neutral atoms in addition to the ions, which provides to two key advantages. First, it would simplify the modeling of scattering from surfaces that tend to neutralize the projectile ions. Second, it would yield a larger signal to projectile-ion-fluence ratio so that insulating surfaces, as well as delicate surfaces prone to damage from sputtering, could be better studied.

ACKNOWLEDGMENTS

C.S.W., R.D.K., and J.A.W. acknowledge support from the U.S. Department of Energy Office of Fusion Energy Sciences, through the Materials and Fusion Nuclear Science program. Sandia National Laboratories is a multimission laboratory managed and operated by National Technology and Engineering Solutions of Sandia LLC, a wholly owned subsidiary of Honeywell International Inc., for the U.S. Department of Energy's National Nuclear Security Administration under Contract No. DE-NA0003525. Z.J.B. and B.D.W. acknowledge partial support for this work from the plasma surface interactions project of the Scientific Discovery through Advanced Computing (SciDAC) program, which is jointly funded by the Fusion Energy Sciences (FES) and Advanced Scientific Computing Research (ASCR) programs, and partially supported by FES Grant No. DE-SC-0006661 within the U.S. Department of Energy Office of Science. Computing resources supporting the results presented in this paper were obtained at the National Energy Research Scientific Computing Center (NERSC), a DOE Office of Science User Facility supported by the U.S. Department of Energy under Contract No. DE-AC02-05CH11231. ORNL is managed by UT-Battelle, LLC, for the U.S. Department of Energy under Contract No. DE-AC05-00OR22725.

-
- [1] L. Schlapbach and A. Züttel, *Nature (London)* **414**, 353 (2001).
 - [2] J. Capelle, J. Gilgert, I. Dmytrakh, and G. Pluvinaige, *Int. J. Hydrogen Energy* **33**, 7630 (2008).
 - [3] J. Roth and K. Schmid, *Phys. Scr.* **T145**, 014031 (2011).
 - [4] M. Y. Ye, H. Kanehara, S. Fukuta, N. Ohno, and S. Takamura, *J. Nucl. Mater.* **313–316**, 72 (2003).
 - [5] Y. Ueda, J. W. Coenen, G. De Temmerman, R. P. Doerner, J. Linke, V. Philipps, and E. Tsitrone, *Fusion Eng. Des.* **89**, 901 (2014).
 - [6] M. Wirtz, J. Linke, G. Pintsuk, J. Rapp, and G. M. Wright, *J. Nucl. Mater.* **420**, 218 (2012).
 - [7] M. Wirtz, S. Bardin, A. Huber, A. Kreter, J. Linke, T. W. Morgan, G. Pintsuk, M. Reinhart, G. Sergienko, I. Steudel, G. D. Temmerman, and B. Unterberg, *Nucl. Fusion* **55**, 123017 (2015).
 - [8] R. A. Causey, *J. Nucl. Mater.* **300**, 91 (2002).
 - [9] A. Loarte, B. Lipshultz, A. S. Kukushkin, G. F. Matthews, P. C. Stangeby, N. Asakura, G. F. Counsell, G. Federici, A. Kallenbach, K. Krieger *et al.*, *Nucl. Fusion* **47**, S203 (2007).

- [10] J. Roth, E. Tsitrone, T. Loarer, V. Philipps, S. Brezinsek, A. Loarte, G. F. Counsell, R. P. Doerner, K. Schmid, O. V. Ogorodnikova, and R. A. Causey, *Plasma Phys. Controlled Fusion* **50**, 103001 (2008).
- [11] Z. A. Piazza, M. Ajmalghan, Y. Ferro, and R. D. Kolasinski, *Acta Mater.* **145**, 388 (2018).
- [12] Z. J. Bergstrom, C. Li, G. D. Samolyuk, B. P. Uberuaga, and B. D. Wirth, *J. Phys.: Condens. Matter* **31**, 255002 (2019).
- [13] T. Carlson, *Photoelectron and Auger Spectroscopy* (Plenum Press, New York, 1975).
- [14] D. M. Mattox, *Physical Vapor Deposition (PVD) Processing*, 2nd ed. (Elsevier, Oxford, UK, 2010).
- [15] J. Grant, *Surf. Interface Anal.* **14**, 271 (1989).
- [16] G. Binnig and H. Rohrer, *Surf. Sci.* **126**, 236 (1983).
- [17] M. A. Van Hove, W. H. Weinberg, and C.-M. Chan, *Low-Energy Electron Diffraction: Experiment, Theory, and Surface Structure Determination* (Springer-Verlag, Berlin, 1986).
- [18] A. C. Dillon, K. M. Jones, T. A. Bekkedahl, C. H. Klang, D. S. Bethune, and M. J. Heben, *Nature (London)* **386**, 377 (1997).
- [19] A. M. Baro and W. Erley, *Surf. Sci.* **112**, L759 (1981).
- [20] M. M. Coleman, D. J. Skrovanek, J. Hu, and P. C. Painter, *Macromolecules* **21**, 59 (1988).
- [21] G. Benedek and J. P. Toennies, *Surf. Sci.* **299–300**, 587 (1994).
- [22] D. Farías and K.-H. Rieder, *Rep. Prog. Phys.* **61**, 1575 (1998).
- [23] K.-H. Rieder and T. Engel, *Phys. Rev. Lett.* **45**, 824 (1980).
- [24] K.-H. Rieder and W. Stocker, *Surf. Sci.* **164**, 55 (1985).
- [25] E. Hulpke and J. Lüdecke, *Surf. Sci.* **272**, 289 (1992).
- [26] D. Farías, M. Patting, and K. H. Reider, *J. Chem. Phys.* **117**, 1797 (2002).
- [27] D. S. Kaufman, L. R. Allen, E. H. Conrad, R. M. Aten, and T. Engel, *Surf. Sci.* **173**, 517 (1986).
- [28] R. Bastasz, T. E. Felter, and W. P. Ellis, *Phys. Rev. Lett.* **63**, 558 (1989).
- [29] O. Grizzi, J. Gayone, G. Gómez, R. Pregliasco, and E. Sánchez, *J. Nucl. Mater.* **248**, 428 (1997).
- [30] R. D. Kolasinski, N. C. Bartelt, J. A. Whaley, and T. E. Felter, *Phys. Rev. B* **85**, 115422 (2012).
- [31] R. D. Kolasinski (unpublished).
- [32] R. D. Kolasinski (unpublished).
- [33] N. A. W. Holzwarth, J. A. Chervenak, C. J. Kimmer, Y. Zeng, W. Xu, and J. Adams, *Phys. Rev. B* **48**, 12136 (1993).
- [34] P. Hadzel, L. Jurczyszyn, and R. Kucharczyk, *Surf. Sci.* **603**, 2507 (2009).
- [35] R. G. Agostino, P. Aebi, J. Osterwalder, J. Hayoz, and L. Schlapbach, *Surf. Sci.* **384**, 36 (1997).
- [36] R. D. Kolasinski, J. A. Whaley, and R. Bastasz, *Phys. Rev. B* **79**, 075416 (2009).
- [37] P. W. Tamm and L. D. Schmidt, *J. Chem. Phys.* **54**, 4775 (1971).
- [38] R. Bastasz, J. A. Whaley, T. A. Lograsso, and C. J. Jenks, *Philos. Mag.* **86**, 855 (2006).
- [39] R. D. Kolasinski, J. A. Whaley, and D. K. Ward, *Surf. Sci.* **677**, 176 (2018).
- [40] W. Eckstein and R. Bastasz, *Nucl. Instrum. Methods Phys. Res. Sect. B* **29**, 603 (1988).
- [41] H. Niehus, W. Heiland, and E. Taglauer, *Surf. Sci. Rep.* **17**, 213 (1993).
- [42] R. Bastasz and J. A. Whaley, *J. Nucl. Mater.* **337–339**, 544 (2005).
- [43] M. T. Robinson and I. M. Torrens, *Phys. Rev. B* **9**, 5008 (1974).
- [44] See Supplemental Material at <http://link.aps.org/supplemental/10.1103/PhysRevB.100.245405> for MD simulations of the W(QS) signal, additional information about shadow cones and shadow lines, details on the vibrational analysis to obtain the Debye temperature, a plot of R factors for the hydrogen adsorbate height and position modeling, and Ref. [57].
- [45] M. A. Karolewski, *Nucl. Instrum. Methods Phys. Res. Sect. B* **230**, 402 (2005).
- [46] M. Aono, C. Oshima, S. Zaima, S. Otani, and Y. Ishizawa, *Jpn. J. Appl. Phys.* **20**, L829 (1981).
- [47] G. Kresse and J. Hafner, *Phys. Rev. B* **47**, 558 (1993).
- [48] G. Kresse and J. Furthmüller, *Phys. Rev. B* **54**, 11169 (1996).
- [49] L. Clarke and L. Morales de la Garza, *Surf. Sci.* **99**, 419 (1980).
- [50] M. Debe, D. A. King, and F. Marsh, *Surf. Sci.* **68**, 437 (1977).
- [51] C. Waldfried, D. McIlroy, J. Zhang, P. Dowben, G. Katrich, and E. Plummer, *Surf. Sci.* **363**, 296 (1996).
- [52] J. F. Ziegler, J. P. Biersack, and U. Littmark, *The Stopping and Range of Ions in Solids* (Pergamon Press, New York, 1985).
- [53] T. E. Felter, E. C. Sowa, and M. A. Van Hove, *Phys. Rev. B* **40**, 891 (1989).
- [54] V. Violante, A. Basile, and E. Drioli, *Fusion Eng. Des.* **22**, 257 (1993).
- [55] B. D. Adams and A. Chen, *Mater. Today* **14**, 282 (2011).
- [56] M. Walker, M. G. Brown, M. Draxler, L. Fishwick, M. G. Dowsett, and C. F. McConville, *Surf. Sci.* **605**, 107 (2011).
- [57] T. H. Seng and M. A. Karolewski, *Nucl. Instrum. Methods Phys. Res. Sect. B* **73**, 163 (1993).